Anion Vacancy Regulated Sodium/Potassium Intercalation in Potassium Prussian Blue Analog Cathodes for Hybrid Sodium-Ion Batteries

Runzhe Wei, Xingwu Zhai, Henry R. Tinker, Pan He, Charlie A. F. Nason, Yupei Han, Veronica Celorrio, Gopinathan Sankar, Min Zhou,* and Yang Xu*

Fe-based potassium Prussian blue analogs (K-PBAs) are commonly used as K-ion battery (KIB) cathodes. Interestingly, K-PBAs are appealing cathodes for Na-ion batteries (NIBs). In a hybrid NIB cell, where Na-ion is in the electrolyte and K-ion is in the PBA cathode, cation intercalation and electrochemical performance of the cathode can be significantly affected by $[Fe(CN)6]^{4-}$ anion vacancy. This work studies the effect of anion vacancy in K-PBAs on regulating K-ion/Na-ion intercalation mechanism in hybrid NIB cells, by comparing two K-PBA cathodes with different vacancy contents. The results demonstrate that introducing a level of anion vacancy can maximize the number of K-ion intercalation sites and enhance K-ion diffusion in the PBA framework. This facilitates K-ion intercalation and suppresses Na-ion intercalation, resulting in a K-ion-dominated and high-discharge-voltage ion storage process in the hybrid NIB cell. The K-PBA cathode with 20% anion vacancy delivers 128 mAh g^{-1} at 25 mA g^{-1} and 67 mAh g^{-1} at 1000 mA g^{-1}, as well as retains 89% and 81% capacity after 100 and 300 cycles, respectively. It completely outperforms the counterpart with 7% anion vacancy, which exhibits increased Na-ion intercalation but overall deteriorated ion storage.

R. Wei, H. R. Tinker, P. He, C. A. F. Nason, Y. Han, G. Sankar, Y. Xu
Department of Chemistry
University College London
London WC1H 0AJ, UK
E-mail: y.xu.1@ucl.ac.uk
X. Zhai, M. Zhou
Hefei National Research Center for Physical Sciences at the Microscale
School of Chemistry and Materials Science
University of Science and Technology of China
Hefei, Anhui 230026, China
E-mail: mzchem@ustc.edu.cn
V. Celorrio
Diamond Light Source
Harwell Science and Innovation Campus
Didcot OX11 0DE, UK

1. Introduction

Na-ion batteries (NIBs) are a technological analog to Li-ion batteries (LIBs) but with several competitive benefits,[1] including economic benefits stemming from the low cost of sodium resources and the possibility of employing Al as the anode current collector and chemical benefits of the lower desolvation energy of Na$^+$ in polar solvents and the better interfacial kinetics at the electrode/electrolyte interface, compared with Li$^+$.[2–4] The large size of Na$^+$ poses a challenge for developing NIB cathodes that allow reversible Na$^+$ intercalation and fast Na$^+$ diffusion.[5,6] Prussian blue analogs (PBAs) have been explored as a family of NIB cathodes.[7–9] The framework of Na$^+$-filled PBAs (Na-PBAs), with a general formula Na$_x$M[Fe(CN)$_6$]$_{1-y}$·zH$_2$O ($0 < x \leq 2$, $0 < y \leq 1$, $z < 2$, M = transition metal), has large interstitial sites to accommodate Na$^+$ and directional channels for fast Na$^+$ diffusion, as well as the structural "openness" to realize small lattice strain during repetitive Na$^+$ intercalation. As a result, Na-PBAs have delivered some of the best cathode performance for NIBs so far.[10–13] Interestingly, bigger K$^+$-filled PBAs (K-PBAs), with a similar formula K$_x$M[Fe(CN)$_6$]$_{1-y}$·zH$_2$O, were initially studied as cathode materials for K-ion batteries (KIBs),[14–16] but have also been demonstrated to be appealing cathode materials for NIBs,[17–20] delivering a comparable capacity to Na-PBAs. It has been speculated that using K-PBAs as cathodes for NIBs is an attractive approach because compared with Na$^+$, the bigger K$^+$ can better fit the large interstitial voids in the PBA framework, enabling higher structural stability.[14,17,21]

In a hybrid battery system containing two cation species, where K$^+$ residues in a K-PBA cathode and Na$^+$ are present in the electrolyte, the cation intercalation mechanism has been elusive. It is empirically expected that K$^+$ would be extracted from the PBA framework after initial deintercalation, and Na$^+$ would gradually replace K$^+$ in the following intercalation processes, which essentially transforms a K-PBA cathode to a Na-PBA cathode. Such kind of Na$^+$-K$^+$ exchange has been reported,[17] where 50% of K in a KMnFe-PBA (M = Mn) cathode was substituted by Na after 30 cycles in a NIB cell. In contrast, no significant Na$^+$-K$^+$

exchange was observed in the initial cycles of a KFeFe-PBA (M = Fe) cathode,[19] but the result of long-term cycles remained unknown. Noting that theoretical simulations have demonstrated the strong dependence of cation intercalation in the PBA framework on the ionic radii of the cations, and K^+ intercalation took place at a higher voltage compared with Na^+ intercalation in the same PBA framework, thus potentially providing higher energy density.[22,23] To this end, it is crucial to regulate cation intercalation mechanism of a hybrid NIB cell in a way that maximizes K^+ intercalation and minimizes Na^+ intercalation in a K-PBA cathode, even though the Na concentration in the electrolyte is several folders higher than the K concentration in the K-PBA cathode.

As one of the most important structural complexities of PBAs, $[Fe(CN)_6]^{4-}$ anion vacancy has shown a significant role in various ion batteries.[10,11,24–28] For instance, Komoba's group reported that size effect is not the primary factor, but introducing a suitable number of anion vacancy can enhance K diffusion in the cathode and thus their KIB performance.[26] For the case of NIBs, Regulating K^+/Na^+ intercalation mechanism to realize the increase in intercalation voltage and energy density of hybrid NIBs can be strongly directed by the anion vacancy content in PBAs. To the best of our knowledge, no direct evidence has been provided in literature with regard to the correlation between the $[Fe(CN)_6]^{4-}$ anion vacancy in K-PBAs and K^+/Na^+ intercalation mechanism/K-PBA cathode performance in hybrid NIB cells, impeding the full potential of such an interesting yet promising battery system. Herein, we report the synthesis of KFeFe-PBAs with different $[Fe(CN)_6]^{4-}$ anion vacancy contents by adjusting reaction temperature and the applications of KFeFe-PBAs as cathode materials in hybrid NIBs. A comparative study on the electrochemical performance, cation intercalation mechanism, and cation diffusion kinetics of the cathodes is carried out to understand how anion vacancy content regulates K^+/Na^+ intercalation mechanism. Our results demonstrate that a higher vacancy content enhances reversible K^+ intercalation, which in turn suppresses Na^+ intercalation in the KFeFe-PBA cathodes, realizing the increase in intercalation voltage throughout the discharge process and enhancing cycling stability over a long term. The KFeFe-PBA cathode with 20% $[Fe(CN)_6]^{4-}$ vacancy delivered an initial discharge capacity of 128 mAh g^{-1} at 25 mA g^{-1} and retained 89% and 81% capacity after 100 and 300 cycles, respectively. The cathode exhibited high intercalation voltages at 3.61 and 2.97 V in the hybrid NIB cells, and the voltages were kept throughout the cycles.

2. Results and Discussion

The powder samples synthesized by the potassium citrate-assisted co-precipitation method are denoted as KFeRT and KFe60 to indicate the precipitation at room temperature and 60 °C, respectively. Based on the results of microwave plasma atomic emission spectroscopy (MP-AES) (Table S1, Supporting Information), elemental analysis (Table S2, Supporting Information), and thermogravimetric analysis (TGA) (Figure S1, Supporting Information), the compositions of KFeRT and KFe60 are estimated to be $K_{1.49}Fe[Fe(CN)_6]_{0.8}\cdot1.33H_2O$ and $K_{1.91}Fe[Fe(CN)_6]_{0.93}\cdot0.36H_2O$, respectively, suggesting the $[Fe(CN)_6]^{4-}$ vacancy contents of 20% in the former and 7% in the latter. We examined the crystal structures of the samples by the Rietveld refinement of the X-ray diffraction (XRD) patterns. As shown in **Figure 1**a,b, both patterns can be indexed to a monoclinic KFeFe-PBA phase (space group P2$_1$/n) without crystalline impurities. Based on the compositions, the patterns were successfully fitted with satisfied R values (Tables S3 and S4, Supporting Information), confirming that the estimated compositions and refined structures were reasonably consistent. The lattice parameters of KFeRT were determined to be $a = 10.08876$ Å, $b = 7.26156$ Å, $c = 6.99231$ Å, and $\beta = 90.472°$, and those of KFe60 were $a = 10.06653$ Å, $b = 7.26726$ Å, $c = 6.94713$ Å, and $\beta = 90.235°$. All refined structures were in agreement with typical monoclinic structures of KFeFe-PBAs.[14,29] We use the structural models of $[Fe(CN)_6]^{4-}$ vacancy-containing (KFeVC, inset in Figure 1a) and vacancy-free (KFeVF, inset in Figure 1b) to represent KFeRT and KFe60, respectively, in order to facilitate our discussion. Both samples showed a weak pre-edge peak at 7115.6 eV in the Fe K-edge X-ray absorption near-edge spectra (XANES, Figure S2, Supporting Information), demonstrating the typical octahedrally coordinated environment of the Fe centers.[30] The main absorption peaks are observed at 7131.5 eV for KFeRT and 7130.9 eV for KFe60, being between the peaks of Prussian White (PW) and Berlin Green (BG) references (Figure S3, Supporting Information). In addition, the Fourier transform infrared spectra (FT-IR) of the samples (Figure S4, Supporting Information) show the characteristic vibration modes of $\upsilon(CN)$, $\upsilon(FeC)$, and $\delta(FeCN)$, which are commonly observed from hexacyanoferrates.[31,32] As shown in the scanning electron microscope (SEM) images (Figure 1c,d), both samples consisted of small nanoparticles and exhibited a certain level of agglomeration. The size of primary particles is in ranges of 30–50 nm (Figure 1c) and 50–80 nm (Figure 1d) for KFeRT and KFe60, respectively. The higher anion vacancy content in KFeRT than KFe60 can be indicated by the more irregular shape of the nanoparticles in the former than the latter.[33] Transmission electron microscope (TEM) images (Figure 1e,f) further reveal the irregular shapes of the primary nanoparticles and their agglomeration. High-resolution TEM (HRTEM) images (insets in Figure 1e,f) display clear lattice fringes in both samples. The d spacings of 2.93 Å and 3.45 Å for KFeRT correspond to the (22-2) and (202) planes, respectively. The d spacings of 3.45 and 4.95 Å for KFe60 correspond to the (202) and (020) planes, respectively. The different d spacings are due to the non-uniformly oriented growth of the primary nanoparticles in the samples; nevertheless, the crystalline nature of the nanoparticles can be confirmed. Our compositional and structural analyses reveal that KFeRT and KFe60 have similar structures and non-stoichiometric compositions that contain $[Fe(CN)_6]^{4-}$ anion vacancy, and a lower precipitation temperature leads to a higher vacancy content[7] in KFeRT being approximately three times higher than KFe60 (20% versus 7%). As will be discussed later, increasing vacancy content is crucial to enhance the NIB performance of KFeFe-PBAs.

We next examined the electrochemical performance of KFeRT and KFe60 as cathode materials in Na half-cells, using 1 M NaClO$_4$ in ethylene carbonate:propylene carbonate (EC:PC = 50:50% vol.) as the electrolyte in the voltage range of 2.0–4.3 V (versus Na$^+$/Na). Since the pristine samples were pre-intercalated with K^+ and the electrolyte only contained Na^+, the electrochemical measurement began with a charge process to extract K^+. **Figure 2**a compares the typical Cyclic voltammetry (CV) curves after the initial charging process of both samples. KFeRT exhibits

ADVANCED
SCIENCE NEWS

www.advancedsciencenews.com

ADVANCED
FUNCTIONAL
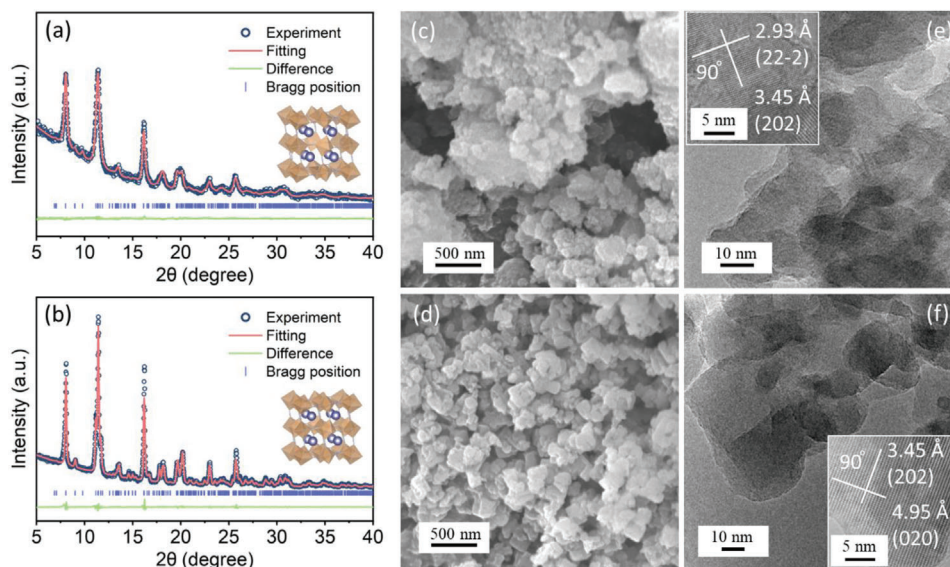**MATERIALS**

www.afm-journal.de

Figure 1. XRD patterns and fitted curves of a) KFeRT and b) KFe60, SEM images of c) KFeRT and d) KFe60, and TEM images of e) KFeRT and f) KFe60 (inset: HRTEM images).

two pairs of redox peaks at 3.54/3.69 and 2.92/3.08 V, corresponding to the redox reactions of C-coordinated low-spin (LS) Fe and N-coordinated high-spin (HS) Fe, respectively, suggesting a two-electron transfer process.[7] Noted that an increase in the intercalation voltages is noticeable in KFeRT (3.54 and 2.92 V) compared to the control sample NaFeRT (3.27 and 2.78 V, Figure S5a, Supporting Information) synthesized by using the same method of KFeRT (Figure S6, Supporting Information). The intercalation voltages of NaFeRT are in good agreement with previously reported Na-PBA cathodes with different particle sizes.[34,35] As will be discussed in the next section, it is K^+ intercalation, instead of Na^+ intercalation, that is responsible for the voltage increase,[18,19,22] even though the amount of Na^+ in the electrolyte is several times higher than the amount of K^+ in KFeRT, and such a difference is caused by the difference anion vacancy contents in the two samples. Interestingly, KFe60 exhibits an extra pair of peaks at 2.78 and 2.92 V. The intercalation voltage (2.78 V) agrees with the voltage at which HS Fe is reduced in NaFeRT (Figure S5a, Supporting Information), which suggests that an extra process of Na^+ intercalation may have occurred. Figure 2b compares the galvanostatic charge–discharge (GCD) profiles after the initial charging process of the two cathodes. The voltages at which discharge plateaus appear agree with the CV results, including the small semi-plateau centering at 2.78 V, which is observed from both KFe60 and NaFeRT (Figure S5b, Supporting Information), once again suggesting a Na^+ intercalation process. The differences in CV and GCD curves between KFeRT and KFe60 are unchanged in the next cycle, with KFe60 exhibiting an extra reduction CV peak and a plateau split (Figure S7, Supporting Information). KFeRT delivered discharge and charge capacities of 128.4 and 139.4 mAh g^{-1}, respectively, at 25 mA g^{-1}, being higher than those of KFe60 (113.5 and 122.5 mAh g^{-1}). Also, KFeRT exhibited great cycling performance (Figure 2c), retaining 114.0 and 103.8 mAh g^{-1} after 100 and 300 cycles at 25 mA g^{-1}, respectively, corresponding to 89% and 81% capacity reten-

tion and completely outperforming KFe60 (64% (72.3 mAh g^{-1}) after 300 cycles). KFeRT delivered 126, 113, 104, 95, 85, 75 and 67 mAh g^{-1} at 50, 100, 200, 300, 500, 750, and 1000 mA g^{-1}, and maintained 112 mAh g^{-1} when being cycled back to 50 mA g^{-1} (Figure 2d). In stark contrast, KFe60 exhibited significant capacity fading from 105 to 78 mAh g^{-1} when current density was increased from 50 to 100 mA g^{-1}. Moreover, the capacity was <50 mAh g^{-1} at higher current densities ($\geq$500 mA g^{-1}). The GCD profiles at various current densities can be found in Figure S8, Supporting Information. Furthermore, KeFeRT retained 72.3 mAh g^{-1} after 700 cycles at 100 mA g^{-1} (Figure 2e), outperforming KFe60 at the same condition (48.3 mAh g^{-1}). Since the main difference between KFeRT and KFe60 is the [Fe(CN)$_6$]$^{4-}$ anion vacancy content, that is, 20% versus 7%, our results indicate that anion vacancy content can affect the cation intercalation mechanism in K-PBAs when they are used as cathodes in NIBs, and as a result, a higher vacancy content can enhance the NIB performance of the K-PBA cathode. How increasing anion vacancy content in K-PBAs regulates Na^+/K^+ intercalation and thus improves NIB performance is not only exciting but also intriguing, because previous literature favored a low anion vacancy content to be a crucial prerequisite for PBA cathodes in NIBs.[10,11,34,35] We are mindful that previous literature discussed NaFeFe-PBAs in this regard, whereas we present here KFeFe-PBAs being used in Na cells, but this makes our results even more exciting and intriguing because to the best of our knowledge, the understanding of the dependence of Na^+/K^+ intercalation on the [Fe(CN)$_6$]$^{4-}$ vacancy content in KFeFe-PBAs has never been reported.

We then draw our attention to cation intercalation processes, as the CV and GCD results have clearly suggested the processes were different between the two samples. We carried out ex situ MP-AES analysis on the KFeRT and KFe60 electrodes at various states of cation (de)intercalation (**Figure 3**a,b) and examined the Na and K contents (normalized to Fe) at each state. Note that
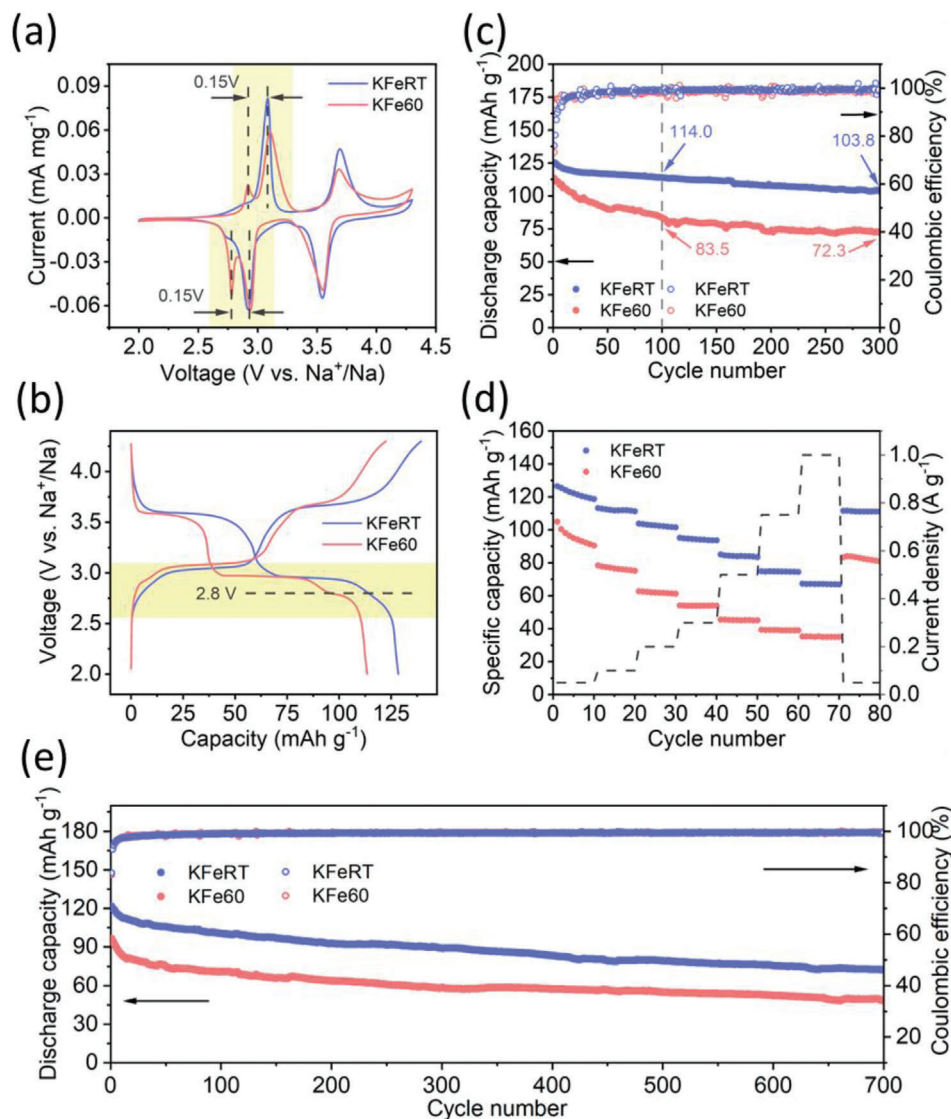
Figure 2. a) CV curves at the scan rate of 0.05 mV s^{-1}, b) GCD profiles and c) cycling performance at 25 mA g^{-1}, d) rate capability, and e) long-term cycling performance at 100 mA g^{-1} of KFeRT and KFe60.

the key difference lies in the discharge/charge plateau split at 2.8 V (state 3)/3.05 V (state 5) for KFe60. In the case of KFeRT (Figure 3c), the Na and K contents increased almost linearly during discharge. However, K$^+$ was the dominating cation, as K/Fe ratio was 0.55 after the first discharge plateau (state 2) and further increased to 0.91 at the end of discharge (state 3). K/Fe ratio was consistently and significantly higher than Na/Fe ratio (0.13 at state 2 and 0.21 at state 3). The K-dominated intercalation seen here confirms the selectivity of the PBA framework toward K$^+$ rather than Na$^+$ and explains the higher intercalation voltages in this work compared with the voltages of NaFeRT and the NaFeFe-PBA cathode in literature.[10,11,34,35] A reverse change of the K/Fe and Na/Fe ratios was observed during the following charge (states 4 and 5). In the case of KFe60 (Figure 3d), K$^+$ dominated the intercalation before the plateau spitting at 2.8 V (state 3). But a sharp increase in Na/Fe ratio ap-

peared after the split, and the ratio peaked at 0.34 at the end of discharge (state 4), whereas the K/Fe ratio remained nearly unchanged from states 3 to 4. This suggests that Na$^+$ was the dominating cation and responsible for the semi-plateau between 2.8 and 2.5 V (Figure 3b). Subsequently, a sharp decrease in Na/Fe ratio appeared during charge between states 4 and 5, while the K/Fe ratio remained nearly unchanged. A sharp decrease in K/Fe ratio appeared during the rest of charge between states 5 and 7, while the Na/Fe ratio remained very low. Additionally, we carried out ex situ energy dispersive X-ray spectroscopy (EDS) measurement on the electrodes (Figure S9, Supporting Information). The K/Fe and Na/Fe ratios agree reasonably well with those obtained from the MP-AES measurement, showing the same changing trends of the ratios during the discharge and charge processes. Therefore, despite a higher initial K$^+$ content in KFe60 than KFeRT (1.91 versus 1.49 per formula), the lower anion vacancy
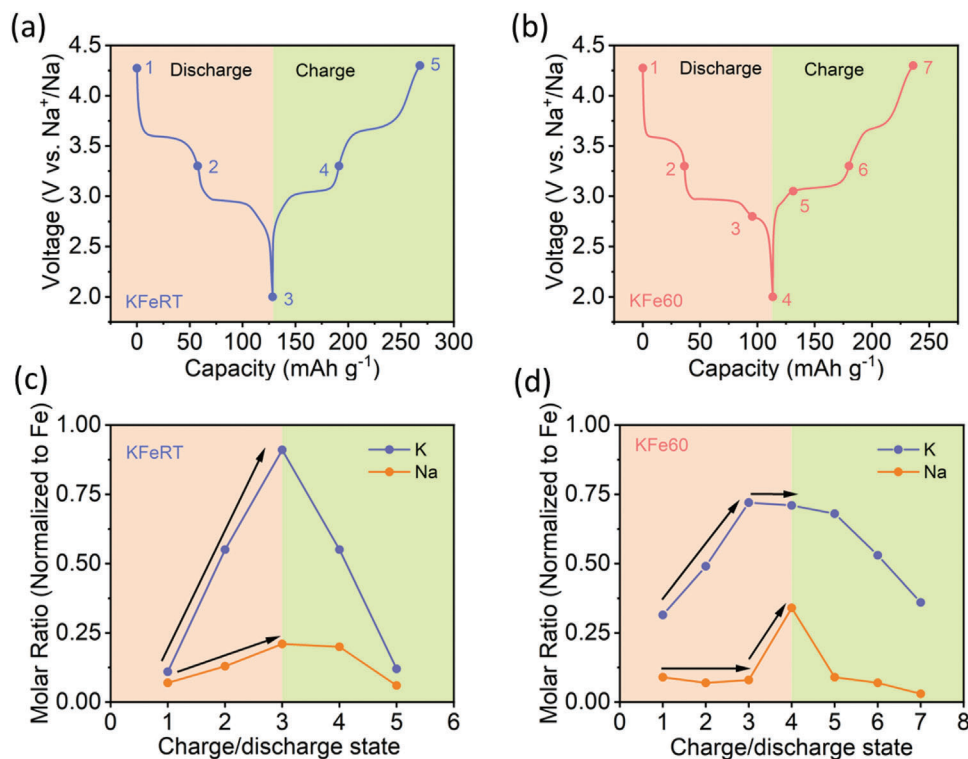
2308227 (4 of 10)

**ADVANCED
SCIENCE NEWS**

www.advancedsciencenews.com

**ADVANCED
FUNCTIONAL
MATERIALS**

www.afm-journal.de

Figure 3. Illustration of the different states of a) KFeRT and b) KFe60 during the first discharge process and the second charge processes. The Na and K contents (normalized to Fe) obtained from MP-AES of c) KFeRT and d) KFe60 at the different states shown in (a) and (b).

resulted in less K⁺ (de)intercalation in KFe60 than KFeRT and an additional Na-dominated intercalation in KFe60. Combining the analysis from KFeRT, the results further confirm that anion vacancy content in KFeFe-PBAs can regulate Na^+/K^+ intercalation, and a lower vacancy content limits K⁺ intercalation,[36] and starts promoting Na⁺ intercalation, being different from previous work.[19]

We tested the KFeRT and KFe60 electrodes after long-term cycles to verify the consistency of the K-dominated intercalation of KFeRT and the increased intercalation of KFe60 below 2.8 V. Table S5, Supporting Information shows the K/Fe and Na/Fe ratios after 300 discharge processes, in comparison to the ratios after 1 discharge process (state 3 for KFeRT in Figure 2c and state 5 for KFe60 in Figure 2d). The K/Fe ratio of KFeRT is consistently high over 300 cycles, suggesting no significant Na⁺-K⁺ exchange occurred during long-term cycling. The Na/Fe ratio of KFe60 is consistently higher than that of KFeRT, suggesting the increased Na⁺ intercalation below 2.8 V is reversible. The XRD patterns of the two samples remain unchanged from the first to the 300th discharge process (Figure S10, Supporting Information). Due to the consistency of K⁺-dominated intercalation, the discharge plateaus of KFeRT remain unchanged after 100 cycles compared to the initial discharge, still showing a ≈0.2 V voltage increase compared to NaFeRT at the 100th discharge (Figure S11, Supporting Information). These results proved that the reversible K-dominated intercalation in KFeRT is promoted by a high anion vacancy content, and more importantly, it is, as far as we know, the first reported evidence of long-term reversible K⁺ (de)intercalation of KFeFe-PBAs used as NIB

cathodes, which is different from the previous results observed from KMnFe-PBAs.[17] In addition, we employed a series of characterization techniques to characterize the KFeRT and KFe60 electrodes at difference discharge and charge states, in order to examine whether various anion vacancy contents may vary the phase transition and/or structural change, which may in turn affect Na^+/K^+ intercalation mechanism. The collective results from the XRD (Figure S12a,b, Supporting Information), Raman (Figure S12c,d, Supporting Information), and X-ray absorption spectroscopy (XAS) analysis (Figures S13–S16, Supporting Information) demonstrate that KFeRT and KFe60 exhibited the same cubic-to-monoclinic phase transition and structural change during discharge (cation intercalation), accompanying the reduction of Fe, and the phase transition was reversible for both samples. It is worth mentioning that Na K-edge XAS results (Figure S17, Supporting Information) further supported the cation intercalation mechanism concluded from the MP-AES and EDS results, that is, Na content remaining low throughout the discharge-charge cycle of KFeRT (Figure S17a, Supporting Information) but showing reversible change from states 3 to 5 for the case of KFe60 (Figure S17b, Supporting Information). Therefore, the results solidify the determining role of $[Fe(CN)_6]^{4-}$ anion vacancy in regulating cation intercalation and the resulting NIB cell performance.

To further understand the role of anion vacancies, we carried out computational evaluations on Na/K intercalation energy and migration energy via the density functional theory (DFT) calculations and experimental measurements on cation diffusion kinetics. The calculations were performed on the KFeVF and KFeVC

**ADVANCED
SCIENCE NEWS**

www.advancedsciencenews.com

**ADVANCED
FUNCTIONAL
MATERIALS**

www.afm-journal.de

Table 1. Cation intercalation energies (unit: eV) of Na^+ and K^+ in the KFeVC and KFeVF models at 8 different available sites.

KFeVC	Site 1	Site 2	Site 3	Site 4	Site 5	Site 6	Site 7	Site 8
K	−0.61	−0.68	−0.53	−0.85	−1.05	−0.73	−0.98	−0.91
Na	−0.10	−0.03	0.07	−0.20	−0.34	−0.18	−0.10	−0.26

KFeVF	Site 1	Site 2	Site 3	Site 4	Site 5	Site 6	Site 7	Site 8
K	−3.95	−3.96	−3.91	−2.46	−4.13	−2.48	−3.99	−3.97
Na	−3.31	−3.37	−3.24	−3.20	−3.41	−3.29	−3.15	−3.24

models, as previously mentioned in Figure 1a,b, to represent KFe60 and KFeRT, respectively. Since the major difference of cation intercalation between the two samples occurs during the low-voltage intercalation (Figures 2 and 3), energies were calculated at the state of 75% body-centered sites being occupied by K^+ (75% potassiation), meaning that in a $2 \times 2 \times 2$ supercell, 24 of 32 sites are occupied by K^+ and 8 sites are available for cation intercalation (Figure S18, Supporting Information). We first calculated the intercalation energies of Na^+ and K^+ at the 8 sites (denoted as site x, $x = 1–8$, **Table 1**). The KFeVC model has lower intercalation energies for K^+ than Na^+ in all 8 sites, while in the KFeVF model, 2 sites (site 4 and site 6) have lower intercalation energies for Na^+ than K^+. This suggests that the presence of anion vacancy can regulate the cation intercalation in the term of thermodynamics way. It has been reported that PBA framework, when no intercalation site is occupied, has a strong selectivity toward large-sized alkali ions, and as a result, K^+ intercalation is more energetically favorable than Na^+ intercalation.[22,37] However, our results showed that in an anion vacancy-free model, some sites prefer Na^+ occupancy with 75% sites occupied by K^+, as the large size of K^+ could possibly inhibit further K^+ intercalation. Also, we are mindful that K^+ intercalation process requires the migration of K^+, and therefore we calculated the migration energy of K^+ from one body-centered site to the adjacent site along a migration path next to an anion vacancy in the KFeVC model (**Figure 4**a) and the equivalent site in the KFeVF model (Figure 4b). The calculations showed that a migration energy barrier of 1.07 eV is needed for the migration path to be energetically favorable in the KFeVF model (Figure 4c), whereas a lower migration energy barrier, 0.81 eV, is needed in the KFeVC model. The calculation results agree with previous calculations of K^+ diffusion in non-potassiated and fully potassiated K-PBA cathodes.[36] We used Arrhenius plots to experimentally test the migration activation energies, which are obtained by the Nyquist plots at 50, 60, 70, and 80 °C (Figure S20, Supporting Information). KFeRT showed an activation energy of 0.26 eV, which is lower than that of KFe60 (0.46 eV). Although the energy values are different from the calculations, the comparison between KFeRT and KFe60 is consistent. Figure 4d,e displays the galvanostatic intermittent titration technique (GITT) curves and calculated diffusion coefficients during the discharging processes of the samples. In general, KFeRT shows smaller over potentials than KFe60, particularly at the two discharge plateaus. The diffusion coefficient of KFeRT is in the range of $\approx 10^{-11}–10^{-12}$ cm^2 s^{-1}, being 1–2 magnitudes higher than that of KFe60 ($\approx 10^{-12}–10^{-14}$ cm^2 s^{-1}). Figure 4f,g shows the CV curves collected at scan

rates from 0.05 to 0.5 mV s^{-1} and the linear fitting is shown in Figure 4h. All the reduction (R) and oxidation (O) peaks are identifiable and reversible, with peak shape almost invariable and the potential differences of the R/O peaks increasing to a small extent when increasing the scan rate. In Figure 4h, the peak currents increase linearly to the square root of the scan rate, suggesting diffusion-controlled reduction (intercalation) and oxidation (deintercalation) processes of both samples. The diffusion coefficients of KFeRT are calculated to be 5.1×10^{-11} and 4.6×10^{-11} cm^2 s^{-1} for R1 and R2, respectively, and 7.1×10^{-11} and 1.4×10^{-11} cm^2 s^{-1} for O1 and O2, respectively. These values are one magnitude higher than those of KFe60, being 6.3×10^{-12} and 5.9×10^{-12} cm^2 s^{-1} for R1 and R2, respectively, and 7.1×10^{-12} and 2.2×10^{-12} cm^2 s^{-1} for O1 and O2, respectively. The results of diffusion coefficient agree reasonably well with the GITT results. Therefore, the computational and experimental results demonstrate that a higher content of $[Fe(CN)_6]^{4-}$ anion vacancy can favor K^+ intercalation from both thermodynamic and kinetics effects; thus, compared with KFe60, K^+ intercalation is maximized in KFeRT, leading to a K-dominated intercalation and a higher capacity in the NIB cell. In addition, a full cell was assembled by pairing KFeRT with a hard carbon anode and using the same Na electrolyte in the half cells, to demonstrate the applicability of KFeRT in hybrid NIBs (Figure S21, Supporting Information). The full cell delivered an initial capacity of 119 mAh g^{-1} at 25 mA g^{-1}, with two discharge plateaus of 3.52 and 2.87 V. The capacity is close to the half-cell capacity, and the discharge plateaus remain reasonably similar to those in the half-cell, considering the discharge voltage of the hard carbon anode. The cell showed great reversibility and rate capability, retaining the capacities of 100 mAh g^{-1} after 150 cycles and 60 mAh g^{-1} at 1 A g^{-1}.

We finally illustrate in **Figure 5** the benefits of $[Fe(CN)_6]^{4-}$ anion vacancy in KFeFe-PBAs used as NIB cathode materials. In the case of an anion vacancy-free KFeFe-PBA framework (KFeVF, Figure 5b), the computational and experimental results indicate a slow K^+ diffusion. This leads to an incomplete K^+ extraction in the initial deintercalation (Figure 3d) and more importantly, the deintercalated K^+ did not fully intercalate back in the framework due to the high K^+ migration energy barrier and the preference of Na^+ at certain intercalation sites (Figure 4c and Table 1). As a result, after the K-dominated intercalation process at the higher voltage range, a Na-dominated intercalation process occurs (Figure 3d), giving rise to a plateau split at the low voltage range (Figure 2a,b) and a low capacity, even though most of the sites in the PBA framework favors K^+ intercalation over
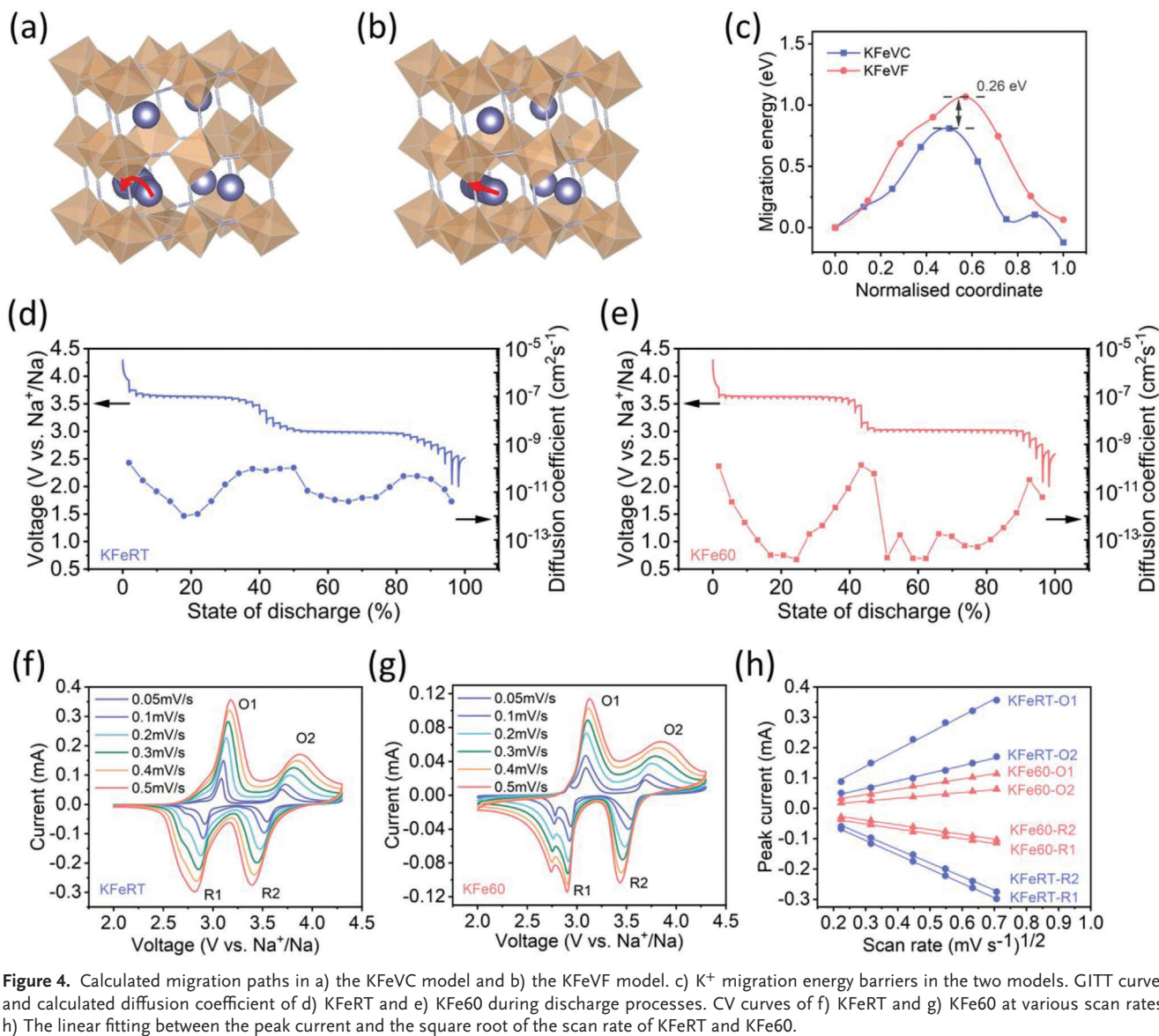
Figure 4. Calculated migration paths in a) the KFeVC model and b) the KFeVF model. c) K^+ migration energy barriers in the two models. GITT curves and calculated diffusion coefficient of d) KFeRT and e) KFe60 during discharge processes. CV curves of f) KFeRT and g) KFe60 at various scan rates. h) The linear fitting between the peak current and the square root of the scan rate of KFeRT and KFe60.

Na^+ intercalation. In contrast, in the case of an anion vacancy-containing KFeFe-PBA framework (KFeVC, Figure 5a), K^+ diffuses faster because of the lower migration energy barrier and the higher diffusion coefficient (Figure 4c,d). This leads to a complete K^+ extraction in the initial deintercalation and the fully reversible K^+ insertion in the following intercalation (Figure 3c). As a result, the two steps of the intercalation process are both dominated by K^+, which enables a high capacity and both the intercalation voltages being higher than those of NaFeFe-PBA cathodes in NIBs (Figure S5, Supporting Information). Therefore, designing defective structures is a crucial approach to regulate the cation intercalation mechanism in a hybrid ion battery system and thus an effective method to enhance the performance of hybrid ion batteries. This approach will be invaluable for hybrid systems in which severely sluggish ion diffusion kinetics take place, such as Mg^{2+} and Ca^{2+} as charge carriers.

3. Conclusions

This work demonstrates the crucial role of $[Fe(CN)_6]^{4-}$ anion vacancy in determining the Na/K intercalation processes in KFeFe-PBAs and their electrochemical performance as the cathode materials in hybrid NIBs. The KFeRT cathode with a higher content of anion vacancy outperforms the KFe60 cathode with a lower content of anion vacancy, by delivering an initial discharge capacity of 128 mAh g^{-1} at 25 mA g^{-1} and retaining 89% and 81% capacity after 100 and 300 cycles, respectively, as well as 67 mAh g^{-1} at 1000 mA g^{-1}. Electrochemical measurements and DFT calculations reveal that the presence of anion vacancy further promotes K^+ intercalation over Na^+ intercalation, reduces K^+ migration energy barrier, and enhances ion diffusion kinetics, which results in the K^+ dominated intercalation at both high and low voltage plateaus while suppressing Na^+ intercalation. The calculations also reveal that K-PBA framework with different anion vacancy

**ADVANCED
SCIENCE NEWS**

www.advancedsciencenews.com

**ADVANCED
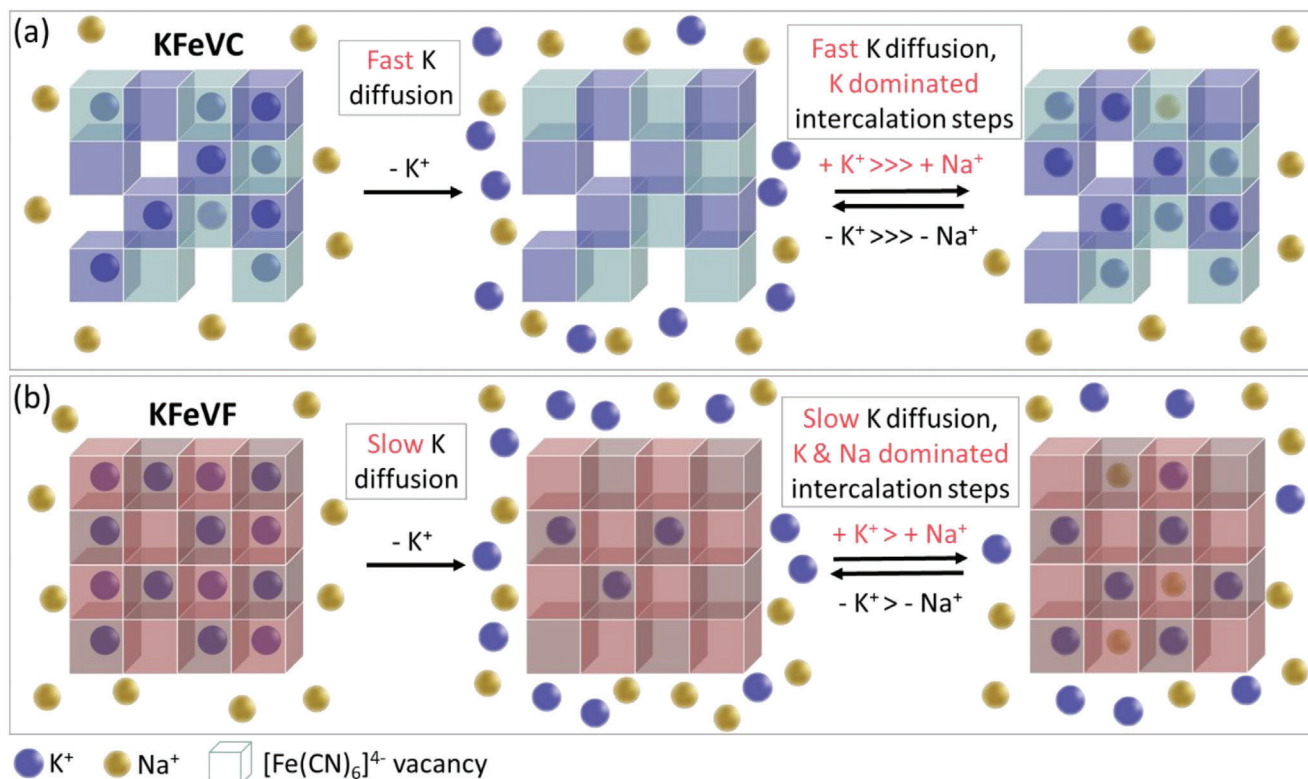FUNCTIONAL
MATERIALS**

www.afm-journal.de

Figure 5. Schematic illustration of cation (de)intercalation in a) the anion vacancy-containing KFeFe-PBA framework and b) the anion vacancy-free KFeFe-PBA framework, when the KFeFe-PBAs are used as cathode materials in NIBs.

levels has different preferences of K/Na intercalation, leading to different cation intercalation behaviors. K-PBAs are an extremely interesting and promising class of cathode materials in Na cells, owing to the preferential insertion of K^+ over Na^+ in the K-PBA framework and the resulting increase in the insertion voltage. Taking full advantage of this kind of hybrid ion batteries requires the understanding of K/Na kinetics and how it plays with varying the structures of K-PBAs. This work highlights that compositional design, including anion vacancy, is the key to enhance the electrochemical performance of hybrid ion batteries.

4. Experimental Section

Materials Synthesis: The KFeFe-PBA samples were synthesized by the potassium citrate-assisted co-precipitation method. First, 2.5 mmol $K_4Fe(CN)_6 \cdot 3H_2O$ and 2.5 mmol $FeSO_4 \cdot 7H_2O$ were separately dissolved into 50 mL 0.2 mol L^{-1} $C_6H_5K_3O_7$ solutions. The two solutions were mixed by slowly dropping the $FeSO_4$ solution into the $K_4Fe(CN)_6$ solution with magnetic stirring. After overnight stirring, the precipitate was centrifuged and washed thoroughly with DI water and isopropanol. Finally, the product was collected after overnight vacuum drying at 60 °C. The samples synthesized at room temperature and 60 °C were donated as KFeRT and KFe60, respectively.

Material Characterizations: The crystalline structure of the powder samples was identified by an X-ray diffractometer (XRD, Stoe STADI P) with Mo Kα radiation ($\lambda = 0.7093$ Å). Rietveld refinements were then conducted using General Structure Analysis System II (GSAS-II). The morphology of the powder samples was observed by a scanning electron microscope (SEM, JEOL JSM-7600F) and a transmission electron microscope (TEM, JEOL JEM-2100). Infrared data was collected using a Fourier transform infrared spectroscopy (Bruker ALPHA compact FT-IR spectrometer). The chemical composition of the samples was collectively determined by thermogravimetric analysis (TGA, Netzsch TG 209 F1 Libra) at a rate of 5 K min^{-1} in nitrogen, microwave plasma atomic emission spectroscopy (MP-AES, Agilent 4210 MP-AES), and elemental analysis (Thermo Flash 2000). The Raman spectra of the electrodes were recorded with 633 nm laser (Renishaw Raman spectrometer). The XRD patterns of the electrodes were obtained by an X-ray diffractometer (XRD, Stoe STADI P) with Cu Kα radiation ($\lambda = 1.5406$ Å). The K/Fe ratio of the electrodes was measured by energy dispersive X-ray spectroscopy (EDS) attached to the SEM. X-ray absorption spectroscopy (XAS) at Fe K-edge were recorded at the B18 beamline of Diamond Light Source (UK) using Si (111) double crystal monochromator. The electrode samples were measured as the original films. The pristine samples and reference samples were pelletized before the measurements. The spectra were collected in fluorescence mode. Data of X-ray absorption near-edge spectra (XANES) and extended X-ray absorption fine structure (EXAFS) was processed using Athena program. XAS at Fe L-edge and Na/K K-edge were recorded at the B07-B beamline of Diamond Light Source (UK). The electrode samples were measured as the original films. The pristine samples and reference samples were pelletized before the measurements. The spectra were collected in the total electron yield mode at a vacuum condition.

Electrochemical Measurements: The working electrodes consisted of 70 wt% KFeFe-PBA sample, 20 wt% Super P, and 10 wt% poly(vinylidene fluoride). This mixture was prepared into a slurry with an optimized amount of 1-methyl-2-pyrrolidone (NMP). The slurry was coated on an aluminum foil using a doctor blade and then vacuum dried at 120 °C overnight. The active material loading was 1.0–1.5 mg cm^{-2}. R2032 type coin cells were assembled in an Ar-filled glove box (water and oxygen concentrations below 0.1 ppm). A sodium disc was used as the counter electrode. A piece of Glass fiber filter was used as the separator. A solution of

1 M NaClO$_4$ dissolved in ethylene carbonate:propylene carbonate (EC:PC = 1:1 in volume) solvent was used as the electrolyte. For full-cell test, the anode consisted of 80 wt% hard carbon, 10 wt% Ketjenblack, and 10 wt% carboxy methylcellulose. The mixture was prepared into a slurry with an optimized amount of deionized water. The slurry was coated on a copper foil using a doctor blade and then vacuum dried at 60 °C overnight. The active material loading was 2.0–3.0 mg cm^{-2}. The cathode/anode mass ratio was 1:2. Galvanostatic charge–discharge (GCD) was carried out on a Neware battery cycler (CT-4008) in a voltage range of 2.0–4.3 V (versus Na$^+$/Na) at room temperature. Cyclic voltammetry (CV) was performed on a Gamry potentiostat (Interface 1010E). The peak currents and square root of the scan rates were fitted by using the Randles–Sevcik equation.[24]

$$i_p = 2.69 \times 10^5 n^{3/2} AC \sqrt{D\nu} \tag{1}$$

where n is the electron transfer number, A represents the interfacial area. (The geometric area was used in this work), C is the concentration of ion, D is the diffusion coefficient and ν is the scan rate.

Electrochemical impedance spectroscopy (EIS) was performed on the same potentiostat with a frequency range of 100 000–0.01 Hz and 1×10^{-5} A rms AC current. Diffusion coefficient was calculated using the following equations.[25]

$$D = \frac{R^2 T^2}{2A^2 n^4 F^4 C^2 \sigma^2} \tag{2}$$

$$Z' = R_e + R_f + R_{ct} + \sigma \omega^{-1/2} \tag{3}$$

where R is molar gas constant (8.314 J mol^{-1} K^{-1}), T is absolute temperature, A is the interfacial area. (The geometric area was used in this work), n is electron transfer number, F is Faraday constant (96 500 C mol^{-1}), C is the concentration of ion, ω is angular frequency and σ is Warburg factor. σ is obtained from the slope of Z' versus $\omega^{-1/2}$ curve.

Galvanostatic intermittent titration technique (GITT) measurement was carried out with a current pulse at 15 mA g^{-1} for 10 min and a 2-h relaxation. Before the measurement, the electrodes were charged and discharged at 15 mA g^{-1} for two cycles. K diffusion coefficient was calculated by the following equation.[26,27]

$$D = \frac{4}{\pi\tau} \left(\frac{n_M V_M}{S}\right)^2 \left(\frac{\Delta V_s}{\Delta V_t}\right)^2 \tag{4}$$

where n_M and V_M are the molar mass and volume of the active material, respectively, τ is the time duration of the current pulse, and S represents the interfacial area. (The geometric area was used in this work). ΔV_s and ΔV_t were obtained from the GITT curves (illustrated in Figure S19, Supporting Information).

Computational Method: All the calculations were performed by applying the spin-polarized DFT method implemented in the Vienna Ab initio Simulation Package (VASP).[28,38] The cut-off energy was set to be 500 eV for the 2 × 2 × 2 KFeFe-PBA supercells. The DFT-D3 method was used to describe van der Waals interactions.[39] The DFT + U method was used to correctly characterize the localization of the Fe d-electrons in the KFeFe-PBA supercells. To differentiate high-spin (HS) and low-spin (LS) Fe ions in the structures, the values of U-J for LS-Fe and HS-Fe were set independently to be 3.0 and 7.0 eV in this work, respectively.[22] During the geometry optimization, the convergence criteria of the force and energy change for all atomic structures were set to be 0.05 eV Å^{-1} and 10^{-5} eV, respectively. The minimum energy pathway search of ion migration was conducted with the climbing image nudged elastic band (CI-NEB) method.[40] The intercalation energy (E_i) of the cations was given by

$$E_i = E_{M@KFeFe-PBA} - E_{KFeFe-PBA} - E_M \tag{5}$$

where M is Na$^+$ or K$^+$, $E_{KFeFe-PBA}$ and $E_{M@KFeFe-PBA}$ are total DFT energies before and after Na/K intercalation, respectively, and E_M is the energy of Na/K ions in its crystal structure.

Supporting Information

Supporting Information is available from the Wiley Online Library or from the author.

Conflict of Interest

The authors declare no conflicts of interest.

Data Availability Statement

The data that support the findings of this study are available from the corresponding author upon reasonable request.

[1] C. Vaalma, D. Buchholz, M. Weil, S. Passerini, *Nat. Rev. Mater.* **2018**, *3*, 18013.

[2] M. Okoshi, Y. Yamada, A. Yamada, H. Nakai, *J. Electrochem. Soc.* **2013**, *160*, A2160.

[3] Y. Yamada, Y. Iriyama, T. Abe, Z. Ogumi, *Langmuir* **2009**, *25*, 12766.

[4] Y. Yamada, Y. Koyama, T. Abe, Z. Ogumi, *J. Phys. Chem. C* **2009**, *113*, 8948.

[5] N. Yabuuchi, K. Kubota, M. Dahbi, S. Komaba, *Chem. Rev.* **2014**, *114*, 11636.

[6] J.-Y. Hwang, S.-T. Myung, Y.-K. Sun, *Chem. Soc. Rev.* **2017**, *46*, 3529.

[7] A. Zhou, W. Cheng, W. Wang, Q. Zhao, J. Xie, W. Zhang, H. Gao, L. Xue, J. Li, *Adv. Energy Mater.* **2021**, *11*, 2000943.

[8] K. Hurlbutt, S. Wheeler, I. Capone, M. Pasta, *Joule* **2018**, *2*, 1950.

[9] B. Xie, B. Sun, T. Gao, Y. Ma, G. Yin, P. Zuo, *Coord. Chem. Rev.* **2022**, *460*, 214478.

[10] X. Wu, M. Sun, S. Guo, J. Qian, Y. Liu, Y. Cao, X. Ai, H. Yang, *ChemNanoMat* **2015**, *1*, 188.

[11] Y. You, X.-L. Wu, Y.-X. Yin, Y.-G. Guo, *Energy Environ. Sci.* **2014**, *7*, 1643.

[12] Y. Xi, Y. Lu, *J. Power Sources* **2021**, *513*, 230554.

ADVANCED
SCIENCE NEWS

www.advancedsciencenews.com

ADVANCED
FUNCTIONAL
MATERIALS

www.afm-journal.de

[13] Y. You, X. Yu, Y. Yin, K.-W. Nam, Y.-G. Guo, *Nano Res.* **2015**, *8*, 117.

[14] X. Bie, K. Kubota, T. Hosaka, K. Chihara, S. Komaba, *J. Mater. Chem. A* **2017**, *5*, 4325.

[15] A. Eftekhari, *J. Power Sources* **2004**, *126*, 221.

[16] C. Zhang, Y. Xu, M. Zhou, L. Liang, H. Dong, M. Wu, Y. Yang, Y. Lei, *Adv. Funct. Mater.* **2017**, *27*, 1604307.

[17] A. Zhou, Z. Xu, H. Gao, L. Xue, J. Li, J. B. Goodenough, *Small* **2019**, *15*, 1902420.

[18] M. J. Piernas-Muñoz, E. Castillo-Martínez, O. Bondarchuk, M. Armand, T. Rojo, *J. Power Sources* **2016**, *324*, 766.

[19] J.-Y. Liao, Q. Hu, B.-K. Zou, J.-X. Xiang, C.-H. Chen, *Electrochim. Acta* **2016**, *220*, 114.

[20] H. Wang, L. Wang, S. Chen, G. Li, J. Quan, E. Xu, L. Song, Y. Jiang, *J. Mater. Chem. A* **2017**, *5*, 3569.

[21] L. Xue, Y. Li, H. Gao, W. Zhou, X. Lü, W. Kaveevivitchai, A. Manthiram, J. B. Goodenough, *J. Am. Chem. Soc.* **2017**, *139*, 2164.

[22] C. Ling, J. Chen, F. Mizuno, *J. Phys. Chem. C* **2013**, *117*, 21158.

[23] J. Zheng, W. Deng, Z. Hu, Z. Zhuo, F. Liu, H. Chen, Y. Lin, W. Yang, K. Amine, R. Li, *ACS Energy Lett.* **2017**, *3*, 65.

[24] B. Yan, M. Li, X. Li, Z. Bai, J. Yang, D. Xiong, D. Li, *J. Mater. Chem. A* **2015**, *3*, 11773.

[25] W. Choi, H.-C. Shin, J. M. Kim, J.-Y. Choi, W.-S. Yoon, *J. Electrochem. Sci. Technol.* **2020**, *11*, 1.

[26] Z. Shen, L. Cao, C. D. Rahn, C.-Y. Wang, *J. Electrochem. Soc.* **2013**, *160*, A1842.

[27] A. Nickol, T. Schied, C. Heubner, M. Schneider, A. Michaelis, M. Bobeth, G. Cuniberti, *J. Electrochem. Soc.* **2020**, *167*, 090546.

[28] G. Kresse, J. Furthmüller, *Phys. Rev. B* **1996**, *54*, 11169.

[29] L. Deng, J. Qu, X. Niu, J. Liu, J. Zhang, Y. Hong, M. Feng, J. Wang, M. Hu, L. Zeng, Q. Zhang, L. Guo, Y. Zhu, *Nat. Commun.* **2021**, *12*, 2167.

[30] B. Xie, L. Wang, J. Shu, X. Zhou, Z. Yu, H. Huo, Y. Ma, X. Cheng, G. Yin, P. Zuo, *ACS Appl. Mater. Interfaces* **2019**, *11*, 46705.

[31] S. N. Ghosh, *J. Inorg. Nucl. Chem.* **1974**, *36*, 2465.

[32] J. W. Boclair, P. S. Braterman, B. D. Brister, Z. Wang, F. Yarberry, *J. Solid State Chem.* **2001**, *161*, 249.

[33] C. Yan, A. Zhao, F. Zhong, X. Feng, W. Chen, J. Qian, X. Ai, H. Yang, Y. Cao, *Electrochim. Acta* **2020**, *332*, 135533.

[34] Y. Liu, Y. Qiao, W. Zhang, Z. Li, X. Ji, L. Miao, L. Yuan, X. Hu, Y. Huang, *Nano Energy* **2015**, *12*, 386.

[35] W.-J. Li, S.-L. Chou, J.-Z. Wang, Y.-M. Kang, J.-L. Wang, Y. Liu, Q.-F. Gu, H.-K. Liu, S.-X. Dou, *Chem. Mater.* **2015**, *27*, 1997.

[36] T. Hosaka, T. Fukabori, H. Kojima, K. Kubota, S. Komaba, *ChemSusChem* **2021**, *14*, 1166.

[37] A. L. Crumbliss, P. S. Lugg, N. Morosoff, *Inorg. Chem.* **1984**, *23*, 4701.

[38] G. Kresse, D. Joubert, *Phys. Rev. B* **1999**, *59*, 1758.

[39] S. Grimme, J. Antony, S. Ehrlich, H. Krieg, *J. Chem. Phys.* **2010**, *132*, 154104.

[40] G. Henkelman, B. P. Uberuaga, H. Jónsson, *J. Chem. Phys.* **2000**, *113*, 9901.